Composites: Part A 175 (2023) 107766

Contents lists available at ScienceDirect

Composites Part A

journal homepage: www.elsevier.com/locate/compositesa

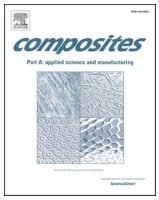

In situ damage characterization of CFRP under compression using high-speed optical, infrared and synchrotron X-ray phase-contrast imaging

Nazanin Pournoori [a,*], Guilherme Corrêa Soares [a], Bratislav Lukić [b], Matti Isakov [a], Maria Clara Lessa Belone [a], Mikko Hokka [a], Mikko Kanerva [a]

[a] Engineering Materials Science, Faculty of Engineering and Natural Sciences, Tampere University, POB 33014, Tampere, Finland
[b] The European Synchrotron Radiation Facility, 38043 Grenoble Cedex 9, France

ARTICLE INFO

Keywords:
Carbon fiber-reinforced polymer composites
Adiabatic heating
High strain rate
Compressive damage

ABSTRACT

The strain rate dependency and failure modes of carbon fiber reinforced plastic (CFRP) laminate were investigated under out-of-plane compressive loading. Simultaneous high-speed optical and infrared imaging were used to measure full-field deformation and temperature in the dynamically loaded specimens. The damage initiation and propagation inside the CFRP laminates at high strain rates were characterized using in-situ ultra-fast synchrotron X-ray phase contrast imaging (XPCI). The visually observed damage onset occurs at the strain value of 4.2 ± 0.6% as a transverse shear fracture at the free edge of specimens. The local temperature increases significantly to 185 °C due to damage initiation at high strain rates, while at low strain rates the temperature rise occurs after the final shear band forms. The XPCI and post-failure analysis provide an integrated perspective on the formation of a diagonal shear crack and disintegration of the specimen into two pieces with the fracture of plies in the in-plane transverse direction. Scanning electron microscopic (SEM) study was integrated with XPCI results to append the time scale for the post-mortem failure pattern as well as the length scale for microcracks and filament-level failure.

1. Introduction

Carbon fiber reinforced polymer (CFRP) laminates are used in different engineering designs, which can be exposed to impact loads due to unexpected collisions. Therefore, a complete understanding of the damage mechanisms of CFRP during impact loading is required for the reliable design of structures. Several experimental techniques, such as servo-hydraulic testing machines, low-velocity drop-weight system, and the Split Hopkinson Pressure Bar (SHPB), have been used and are continuously improved to identify the effects of strain rate on the mechanical response of CFRP [1,2]. A common focus has been given to the study of the failure mechanisms of CFRP under in-plane loading using high-speed cameras and the measurements of in-plane strain fields of the specimens by the digital image correlation (DIC) method [3,4]. The compressive behavior of unidirectional (i.e., axial) CFRP at a high rate has been reported to depend on the fiber volume fraction of the composite, and its stress-strain curves have been characterized by two linear regions of different slopes, but this behavior has not been observed in the out-of-plane tests [5]. The results from the in-plane longitudinal and transverse compressive experiments on unidirectional carbon-epoxy laminates, for a strain rate range of 10^{-4} to 10^{3} s^{-1}, demonstrate that the compressive elastic modulus only in the in-plane transverse direction is strain rate sensitive, while both in-plane longitudinal and transverse compressive strengths increase significantly at higher strain rates [3,6]. Additionally, the compressive in-plane shear stiffness and strength – determined for a ±45° lay-up – increase with increasing strain rate, while the failure strain decreases [7]. Interestingly, experiments on a cross-ply CFRP with 48 plies have shown a significant reduction in the failure strain for in-plane compression from a low strain rate to a high strain rate. This was found to be due to drastic variations in failure modes including kinking, shear failure, and final disintegration of the specimen [8].

The characterization of out-of-plane compressive failure of multi-angle laminates is still a challenge at high strain rates, mainly due to the appearance of different failure modes. The out-of-plane compression of cross-ply CFRP (AS4-PEEK) has shown the occurrence of various failure modes including fiber breakage, matrix failure, crack propagation, delamination, and crushing of fibers and matrix at high strain rates

* Corresponding author.
E-mail address: nazanin.pournoori@tuni.fi (N. Pournoori).

https://doi.org/10.1016/j.compositesa.2023.107766
Received 22 January 2023; Received in revised form 29 May 2023; Accepted 27 August 2023
Available online 1 September 2023

ranging from 1500 s^{-1} to 7000 s^{-1} [9]. The initiation and propagation of various failures are also highly dependent on ply thickness as well as the stacking sequence of laminates under out-of-plane impacts [10,11]. Understanding the effects of realistic lay-ups on the failure onset is important for design purposes and needs further research. X-ray imaging, in particular computed tomography (CT), has proven to be a powerful technique to detect various internal flaws and damage at the length scale of individual plies and broken fibers, which are not visible in planar images of the specimen surface [12,13]. Synchrotron-based CT has been used to analyze damage initiation and evolution, particularly fiber failure in carbon fiber–epoxy laminates in tension, indentation, and fatigue, thus facilitating unprecedented sub-micron spatial resolution [14-17]. However, observations of these failure modes at high strain rate loading necessitate ultra-fast acquisition. In-situ ultra-fast radiography has been recently used to identify damage initiation at a spatial scale of 20 μm and timing scale of 1 μs and to track the crack propagation in glass fiber-reinforced composites using a modified SHPB [18,19]. However, the high rate compression in the out-of-plane direction and related failure modes have not yet been studied for CFRP laminates using in-situ synchrotron X-ray imaging.

The adiabatic temperature-rise caused by mechanical damage is important in understanding different energy dissipation mechanisms in CFRP composites [20]. Ou et al. [21] tested a unidirectional CFRP at intermediate strain rates under in-plane tensile loading, and their results indicated that the failure patterns depend on specimen temperature but not on strain rate. The abrupt temperature rise in CFRP composites under tensile load and impact was mainly observed with fiber breakage, which occurred due to the decreased bonding strength between fibers and matrix [21,22]. However, less adiabatic heating has been observed in CFRP laminates which failed by delamination and plastic deformation [22]. The simultaneous monitoring of deformation and temperature has been carried out for glass fiber-reinforced laminates under out-of-plane compression, and the temperature rise has been shown to depend on the damage mode at high strain rates [23,24].

The primary objective of this study is to investigate the effects of strain rate on adiabatic heating and damage mechanisms of CFRP laminate under out-of-plane compressive loading. The term ‘adiabatic heating’ is here used as an umbrella term to focus on the immediate conversion of (strain) energy into heat when triggered by the various mechanical failure mechanisms of the investigated material. The damage processes of laminate specimens at high strain rates are characterized with synchronized high-speed optical and infrared imaging as well as in-situ ultra-fast synchrotron XPCI. DIC analysis is used to calculate the non-uniform deformation and strain fields on the surface of the specimens, while ultra-fast XPCI provides complementary information about the damage modes observed inside the specimen. The post-failure analysis of the tested specimens is performed using the scanning electron microscope (SEM) to gain detailed information on the damage mechanisms at the micro-scale. Results indicate that the local temperature of the specimen increases significantly after the damage onset at a high strain rate, while the specimen heats up only after the peak force at a low strain rate. The results also indicate a connection between temperature changes and variations in damage modes of the tested specimens at different strain rates.

2. Materials and methods

2.1. Specimen preparation and characterization

The material studied in this work comprised AS4 carbon fibers and 3501-6 epoxy (Hexcel Corp., USA). The composite was laminated in prepreg form and cured via an autoclave process according to the manufacturer’s guidelines. The angle-ply laminate included 28 unidirectional plies (lay-up of $[(0)_3/-45/0/+45/-45/0/+45/0/0/-45/0/+45]_{SE}$) and peel plies on the outer surfaces. Cubic specimens were cut out from the laminate using waterjet cutting. The peel plies on the surfaces were removed by polishing, and the surface parallelism was controlled. The straightness of the surfaces to be in contact with the test anvils was controlled to be within a 10 μm tolerance. The length of each side of the cubic specimens was measured at five points and the average of these measurements was used for determining the individual dimensions per specimen. The nominal side length was 3.9 ± 0.1 mm, as shown in Fig. 1. The specimens were compressed in the out-of-plane direction at strain rates of 10^{-3}, 10^{-2}, and 10^{3} s^{-1}. These tests were repeated at least two times. The effects of the anticipated resin-rich surface (due to peel ply) on the mechanical response were also studied.

2.2. Low and high strain rate tests

The compression tests at low strain rates (10^{-3} and 10^{-1} s^{-1}) were performed using the servo-hydraulic universal testing machine (Instron 8800) with 100 kN load cell (Fig. 2 (a)). For these tests, a clip-on extensometer was attached to the anvils adjacent to the contact surface; this data was used mainly for the relative displacement during compression. The low rate compression tests were recorded using a 5 MPix (Imager E-Lite, LaVision, Germany) low-speed optical camera and a Telops Fast IR M2k high-speed infrared camera (Telops, Canada). The low-speed optical camera was used with a Nikon AF Micro-Nikkor 200 mm f/4D IF-ED lens and the infrared camera was equipped with a 100 mm lens. The low-speed optical camera was connected to the testing machine for synchronizing the force data with the deformation data obtained from DIC.

The high strain rate tests in the out-of-plane direction were performed using the SHPB setups available at the IMPACT Laboratory, Tampere University (TAU), Finland, and at the ID-19 beamline of the European Synchrotron Radiation Facility (ESRF), France. The SHPBs consist of a gas gun, aluminum alloy striker, incident, and transmitted bars, and measurement systems, as summarized in Table 1. At ESRF [25], two maraging steel (Böhler W720, heat treated at 450 °C) discs with a thickness of 4 mm were used at the specimen-bar interfaces to make sure that no damage occurred at the faces of the bars. During the experiment, the air gun accelerates the striker bar to impact the free end of the incident bar and to create a loading pulse that propagates in the incident bar towards the specimen, which is placed between the incident and transmitted bars. Due to the impedance mismatch between the specimen and the pressure bars, a part of the incident pulse is reflected back and a part is transmitted through the specimen into the transmitted bar. The strain and stress in the specimen are calculated from the strain gauge data using the one-dimensional wave propagation theory [26].

The high strain rate compression tests at TAU were monitored using a Photron Fastcam SA-X2 high-speed camera (Photron, Japan) and a Telops Fast IR M2k high-speed infrared camera, as shown in Fig. 2 (b) (see section 2.3). The high-speed camera was used with a Tokina AT-X PROD 100 mm f2.8 Macro lens, and the infrared camera was equipped with a 50 mm lens. At the ID-19 beamline of the ESRF, the determination of the high rate compressive deformation was complemented with an in-situ synchrotron XPCIs, as shown in Fig. 2 (c) (see section 2.4).

2.3. Simultaneous strain and temperature full-field measurements

The optical cameras (see Section 2.2) were used to record the deformation of the patterned surface of the specimen for the calculation of the full-field strains using DIC. Simultaneously, the high-speed infrared camera monitored the clean, non-patterned side of the specimen to measure the full-field surface temperatures using infrared thermography (IRT). For the low strain rate tests, the image acquisition of the optical and infrared cameras was synchronized directly by sending Transistor-Transistor Logic (TTL) pulses from the optical camera to the infrared camera. The infrared images were recorded with an exposure time of 5 μs at a frame rate of 1600 Hz, i.e., 50 times faster than the optical imaging during the low strain rate tests. For the high strain rate tests, a Keysight 33500B function generator was used to

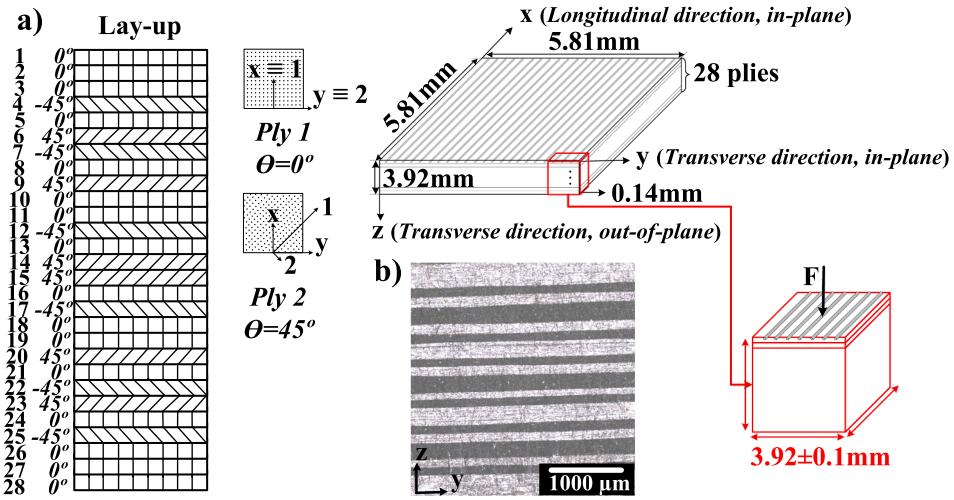

Fig. 1. (a) Schematic pictures including the exact lay-up, cutting, and dimensions of the specimens and (b) a microscope image of the cross-section of a specimen. (For interpretation of the references to colour in this figure legend, the reader is referred to the web version of this article.)

continuously send TTL pulses to clock the optical camera at the desired frequency. A second channel of the function generator was used to send TTL pulses through an analog gate to the infrared camera. When the compressive pulse created by the striker impact and reached the incident bar strain gauge, the oscilloscope was triggered and a TTL pulse was sent to launch the image acquisition of the optical camera and to open the analog gate to begin the image acquisition of the infrared camera. A more detailed description of the synchronization method of the optical and infrared cameras can be found in the work of Soares et al. [27]. The optical camera recorded two times more images than the infrared camera during the high strain rate tests. Table 2 shows the acquisition frame rate and image resolution for both optical and infrared cameras used at tests with different strain rates.

2D strain fields were calculated from the optical images of the specimen surface, specifically the Y-Z-plane (the surface normal to the 0° directed plies), using the 2D-DIC system with DaVis10 software (LaVision Inc, Germany). The average of the local strains over the entire specimen surface was used in the force-strain plots in Figs. 4, 6, and 9. In order to obtain data with high spatial resolution, fine speckles were sprayed on the surface of the CFRP specimens to produce high contrast images, as shown in Figs. 7 and 9. Table 3 shows the processing parameters of the 2D-DIC.

Infrared cameras record the radiometric temperature by assuming that the target material has either the emissivity of a black body or true surface temperature using a user-defined emissivity [27]. Considering that the emissivity depends on many different factors (e.g., material, surface quality, temperature, viewing angle, etc.), the radiometric temperature was converted to the true surface temperature by measuring the temperature of the specimen in two sequences. Firstly, the temperature of a specimen was monitored by both the infrared camera and a K-type thermocouple at room temperature. Secondly, a specimen was partially coated with thermographic paint with known emissivity and slowly heated up to 100 °C using a heat gun. The temperatures of both painted and raw surfaces of the heated specimen were recorded simultaneously with the infrared camera and the thermocouple. The calibration was then determined by linear regression on the data from these two sequences.

2.4. Ultra-fast XPCI

To investigate the fast internal damage progression in CFRP, SHPB experiments were performed using in-situ ultra-fast X-ray imaging at the ID-19 beamline at the ESRF [28] with the instrumentation available through the user programme [25]. The dynamic experiments were performed while the synchrotron operated in the so-called bunch mode, where 16 equally spaced (i.e., 176 ns) and highly populated electron bunches were injected into the storage ring with a nominal current of 75 mA. The hard X-ray pulses of equivalent time spacing were produced by two axially aligned U32 undulators set to a minimum gap, yielding a sufficiently high flux per pulse for single bunch imaging studies [29]. The polychromatic X-ray beam, having a mean energy of about 30 keV, was trimmed along its propagation length and focused onto the specimen using two sets of in-vacuum slits. The experimental hutch was located 145 m downstream from the source. The detector arrangement was also placed 9 m downstream from the specimen. The indirect detector assembly was used, which consists of the Shimadzu HPV-X2 ultra-high speed camera equipped with 210:100 Hasselblad lens arrangement providing 2.1:1 magnification coupled to a 500 µm thick single crystal LYSO:Ce scintillator. The Shimadzu HPV-X2 high sensitivity sensor was used with 400 × 250 effective pixel count and a nominal pixel size of 15.2 µm with on-board memory able to store 128 full frames [30]. The beam setup produced a very large field of view, 4 × 6.4 mm^2. For the experiments presented herein, the detector acquisition was set to 880 ns interframe time with an integration time of 550 ns, hence the temporal resolution is dictated by the camera shutter speed. The 3-bunch integration in one exposure per frame enhances the signal-to-noise per acquired radiograph (here measured to be 25), which is considered a good compromise with respect to temporal resolution. The synchronization of the X-ray train of pulses and the SHPB experiment followed the procedure described in published works [25,31]. A more detailed description of the synchronization of the ultra-fast XPCI system and the SHPB experiment, as used in this study, can be found in the supplementary data.

2.5. Post-failure analysis

The microscopic failure phenomena in the selected specimens were characterized using an SEM JSM-IT500 (Jeol, Japan) under an acceleration voltage of 20 kV. One low strain rate test specimen was cold-mounted with epoxy (Epofix, Struers) and polished to study the failure deeper inside the specimen. One specimen tested at a high strain rate was first attached directly to the stub mounts using conductive carbon cement (Leit-C, Agar), and the fracture surface was imaged. Then, the specimen was cold-mounted and polished similarly to the low rate test specimen. All the surfaces to be studied were coated with 4 nm Pd/Pt using a planar magnetron sputtering device to enhance conductivity during imaging.

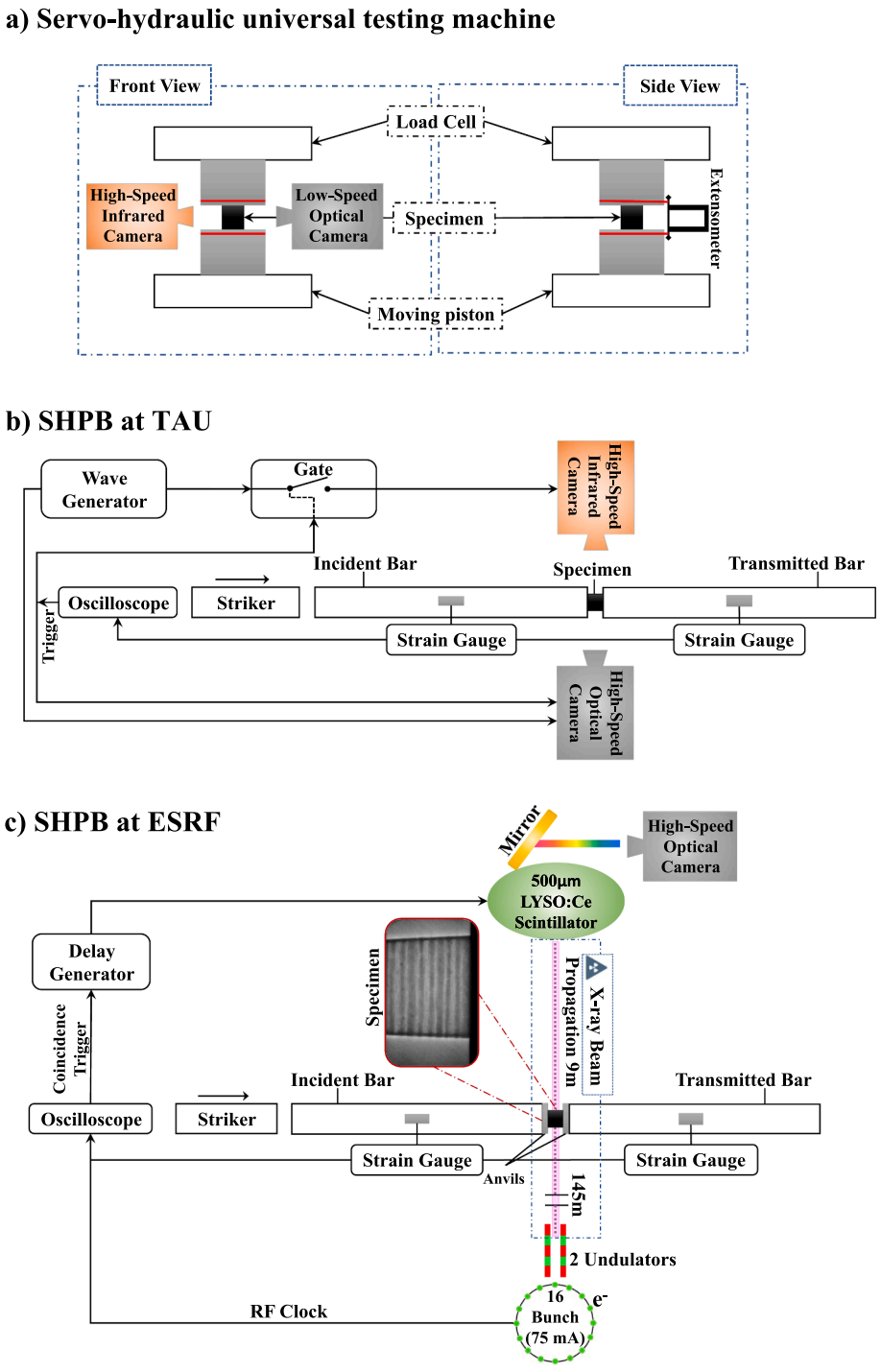

Fig. 2. Schematic illustrations of experimental setups for (a) low strain rate tests and (b) high strain rate tests with optical and infrared cameras at TAU, (c) high strain rate tests with an in-situ synchrotron XPCI used for the in-situ monitoring of the SHPB experiments at ID-19 beamline of the ESRF. (For interpretation of the references to colour in this figure legend, the reader is referred to the web version of this article.)

2.6. Finite element simulations

A 3D finite element model was created using Dassault Systems Simulia Abaqus Standard 6.12 finite element method (FEM) tool to study the effects of lay-up on the stress states of the specimens. The simulations imitating the low strain rate tests included two deformable steel anvils and a specimen with the nominal dimension of 3.92 mm each side. The anvils were placed above and below the specimen by using a surface-to-surface contact formulation without friction. The anvils and the specimen were meshed using the eight-node linear brick elements (C3D8) with a size of 0.1 mm. The boundary conditionrestricted all degrees of freedom on the bottom surface of the lower anvil. The in-plane displacement restrictions were applied also on the top surface of the upper anvil. The in-plane displacements at the middle point and edge point of the bottom surface of the specimen were restricted, as shown in Fig. 3. Finally, an enforced out-of-plane displacement was applied to the upper anvil, and it was equal to the average of experimental displacements of the real specimens at the damage onset. The engineering constants of each CFRP ply were defined as $E_1 = 140$ GPa [32], $E_2 = 10$ GPa [32], $\nu_{12} = 0.3$ [32], $\nu_{13} = 0.3$ [33], $\nu_{23} = 0.52$ [33],

Table 1
SHPBs used at TAU and ESRF laboratories.

Pressure bars information	*TAU*	*ESRF*
Striker length (mm)	300	150
Incident bar length (mm)	1800	1300
Transmitted bar length (mm)	1800	1100
Distance of input gauge to specimen (mm)	600	400
Distance of output gauge to specimen (mm)	600	390
Diameter of the bars (mm)	11.95	12.7
Young's modulus of the bars (GPa)	70.2	73.0
Density of the bars (g/cm^3)	2.70	2.82

Table 2
Frame rate and image resolution of the optical and infrared cameras at tests with different strain rates.

Strain rate (s^{-1})	*Optical camera frame rate (Hz)*	*Optical image resolution (pix)*	*Optical image scale (pix/mm)*	*IR camera frame rate (Hz)*	*IR image resolution (pix)*
$\approx 10^{-3}$ and 10^{-1}	32	790 × 705	178	1600	64 × 64
$\approx 10^{3}$	124,000	256 × 224	41.4	62,000	64 × 16

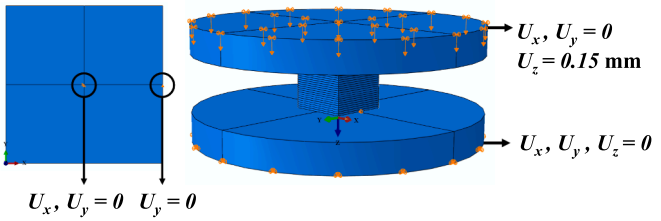

Fig. 3. Boundary conditions and loading are used for the finite element simulation of the specimen under compression. (For interpretation of the references to colour in this figure legend, the reader is referred to the web version of this article.)

G_{12} = 5.17 GPa [32], G_{13} = 5.0 GPa [33], G_{23} = 3.0 GPa [33]. The Young's modulus in the out-of-plane direction was E_3 = 10 GPa and was calculated using the experimentally measured force-displacement responses. The engineering constants of each UD ply were specified in accordance with the local coordinate system (123), where '1' shows the 0° fiber direction.

3. Results

3.1. Rate-dependent mechanical response

The rate-dependent force-strain response of CFRP specimens under out-of-plane compressive loading at three different strain rates (i.e., 10^{-3}, 10^{-1}, and $\approx 10^{3}$ s^{-1}) is presented in Fig. 4 (a). The force-strain curves of the specimens tested at high strain rates are shown in Fig. 4 (b). The average DIC strain in Fig. 4 (a) was obtained as the average full-field strain over the entire specimen surface, while the strain in Fig. 4 (b) was calculated from the reflected strain pulse. This was done to simplify the comparison of the high rate test results at TAU and at ESRF, as DIC was not available for the ESRF experiments.

The experimental and simulated force-strain responses of individual specimens at the low strain rates were compared in Fig. 4 (a), which indicates good agreement between experimental and simulated results in the linear elastic region. Fig. 5 shows the simulated stress field of the specimen estimated for the low strain rate compression. The out-of-plane stress (σ_{zz}) varies as much as 40% at the interfaces of plies with different fiber orientations. This analysis highlights the influence of composite lay-up especially with in-plane free-edge effects on the specimen's stress state. Therefore, the averaged (engineering) stress values of the specimen do not thoroughly represent the stress state in a composite specimen with a lay-up.

In Fig. 4, the designated points ('D') indicate the first visually observed crack in the recorded optical images and synchrotron XPCI results. Damage progression of the CFRP specimens was divided into three phases: damage initiation, damage propagation, and final failure.

3.1.1. Phase I: Linear behavior prior to damage onset

Phase I occurs before the 'D' points in Fig. 4, where the force-strain response indicates linear elastic behavior. The end of Phase I was defined as the average of the strain at the 'D' points of different specimens. The average strain at the 'D' points of the specimens tested at different strain rates was ≈0.042 ± 0.006 mm/mm when the strains were calculated by using DIC, and the 'D' points were found only based on the optical images. The average strain at the 'D' points of the specimens tested at high strain rates was ≈0.035 ± 0.0035 mm/mm when the strain was calculated from the reflected pulse, and the 'D' points were obtained using XPCI and optical images. The slopes of the force-strain curves decreased slightly (less than 15%) with increasing strain rates, as shown in Fig. 4 (a). The comparison of the 'D' points shown in the curves suggests that the strain at this point decreased (<10%) with increasing strain rates as well.

3.1.2. Phase II: Failure propagation after the damage onset

Phase II comprises the material response between the 'D' point and the peak force. During Phase II, the slopes of force-strain curves at low strain rates were only 20% lower than that observed in Phase I. However, the load-carrying capability of the composite decreased significantly in Phase II at high strain rates, which is seen as lower values of force in the force-strain plots and a kink in the slopes of the force-strain curves. Therefore, peak force (along with ultimate strength) decreased with increasing strain rates above a certain strain rate level, as has been similarly reported by Hosur et al. [34]. The force-strain curves obtained at TAU and at ESRF show different details after the 'D' point, which can be related to the differences in experimental setups, causing variations in strain rate and rotation of the specimens. The slight rotation of the specimens can be also attributed to slight errors in the parallelism of bar surfaces and in cutting and polishing of the specimens, or slight changes in the stiffness (e.g., due to the precise distribution of fibers).

3.1.3. Phase III: Final failure

Phase III is the phase after peak (maximum) force. The average of the peak forces was ≈10.8 ± 0.57 kN at low strain rates and was ≈9.0 ± 0.62 kN at high strain rates. The average strain at the peak force points was ≈0.077 ± 0.006 mm/mm when the strains were computed with DIC, and the average strain at the peak force calculated from the reflected pulse was ≈0.083 ± 0.013 mm/mm. Phase III also includes the final brittle failure of the specimen. The force-strain curves from the tests at both low and high strain rates show a sudden decrease in the force due to final failure, as seen in Fig. 4. The failure modes were clearly different at different strain rates, as will be discussed later in Section 3.5 in more detail.

3.2. Strain fields and adiabatic heating at low strain rates

An example of the average and local maximum temperatures on the specimen surface as a function of strain in a low strain rate test is shown in Fig. 6. The measurements indicate that there is no observable heat generation during Phase I of the low strain rate tests. The local maximum temperature and the average temperature did not increase before the start of Phase III. The peak force was followed by gradual failure at the point 3 in Fig. 6, where the local maximum temperature increases slightly (2 °C). Only after the point 3, a dramatic increase in

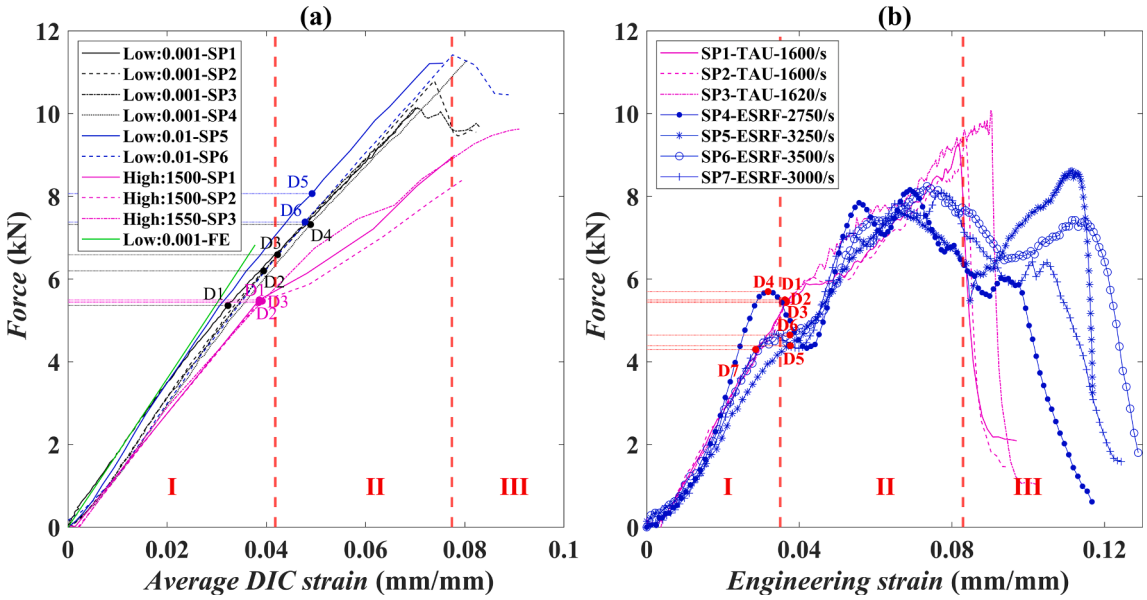

Fig. 4. Out-of-plane compressive force-strain curves of the CFRP laminate specimens (a) at different strain rates (tested at TAU) and calculating an average of the strain over the surface of the specimen using DIC, (b) at a high strain rate (tested at TAU and ESRF) and calculating the strain using the reflected strain pulse. Note: (1) the notation 'SPi' refers to different specimens, (2) the strain rates shown in the figures (a) and (b) were obtained by dividing the strain at the visually observed damage onset by the time it took to reach the given frame. (For interpretation of the references to colour in this figure legend, the reader is referred to the web version of this article.)

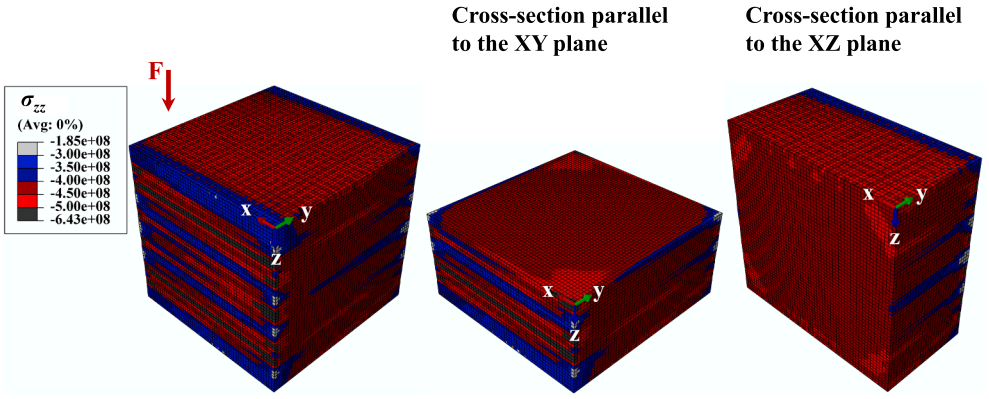

Fig. 5. Simulated out-of-plane stress component (σ_{zz}) of the CFRP specimen under compression. The right-side images show the inside of specimen with the cross-section views. (For interpretation of the references to colour in this figure legend, the reader is referred to the web version of this article.)

Table 3
DIC processing parameters used in this study.

Parameter	*Strain rate (s^{-1})*	
	$\approx 10^{-3}$ and 10^{-1} s^{-1}	*$\approx 10^{3}$ s^{-1}*
Correlation method	Sum-of-differential	Sum-of-differential
Matching criteria	ZNSSD*	ZNSSD*
Subset size	31 pixels	25 pixels
Step size	10 pixels	8 pixels
Subset shape function	Affine	Affine
Interpolation method	6th Order spline function	6th Order spline function
VSG size	165 pixels	41 pixels

*ZNSSD: zero-normalized sum of squared differences.

both local and average temperature occurred due to the final failure. The local maximum temperature exceeded 240 °C abruptly in the tests at the strain rate of 10^{-3} s^{-1}, as highlighted in the right-side curve in Fig. 6. Since the maximum temperature was higher than the glass transition temperature (T_g) of epoxies, the stiffness and local strength of the matrix constituent were expected to deteriorate.

Fig. 7 shows optical images, strain fields, and temperature fields obtained simultaneously from a specimen deformed at the strain rate of 10^{-3} s^{-1}. Visible macroscopic cracks, recorded by the optical camera, nucleated at the free edge of the specimen as shown by the 'D' point (Fig. 7). After the peak force, the localization of strain and heating were clearly observed as the damage evolved diagonally in the specimen, as highlighted at the point 3 in Fig. 7. At the final failure (point 4), a diagonal crack formed approximately at an angle of 45°, thus indicating failure due to shear (i.e., compression and lateral tension due to the Poisson's effect). Finally, the specimen fractured into two pieces. The local temperature increased significantly along the main crack path.

3.3. Characterization of the internal damage at high strain rates

Fig. 8 presents the force as a function of strain, as well as XPCI and optical images recorded during the deformation for the selected high strain rate experiments. The damage onset appeared at the interface of a ply with 0° fiber orientation and a ply with −45° fiber orientation (third and fourth ply from the free edge) close to the anvil, as shown at the 'D'

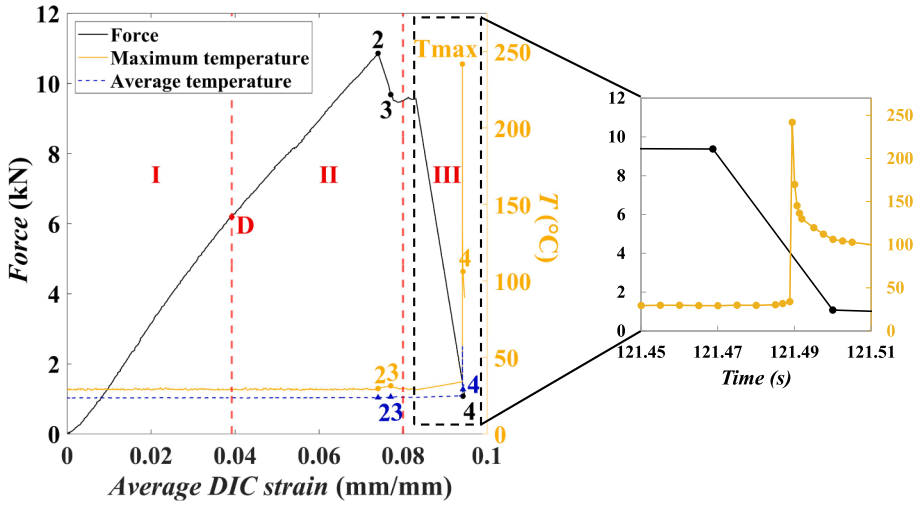

Fig. 6. Force and temperature as a function of strain for the specimen 'SP2' deformed at the strain rate of $10^{-3}\,s^{-1}$. Note: the numbers in the graph are related to the optical and thermal images shown in Fig. 7. (For interpretation of the references to colour in this figure legend, the reader is referred to the web version of this article.)

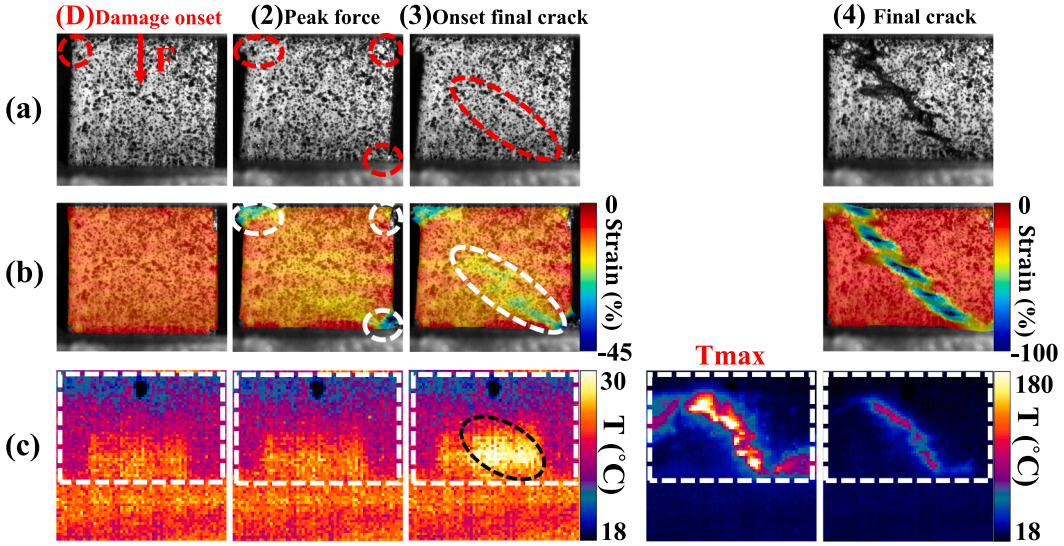

Fig. 7. A sequence of optical images, full-field strain, and temperature maps of damage initiation and propagation at a low strain rate ($\approx 10^{-3}\,s^{-1}$). Note: (1) the loading direction is the vertical direction (red arrow with 'F'), (2) the images in the three rows are sorted by the numbering used in Fig. 6. (For interpretation of the references to colour in this figure legend, the reader is referred to the web version of this article.)

point or in the leftmost column of the XPCI and optical images in Fig. 8. However, the resolution of the images did not allow to conclude whether the damage initiated at the interface of the plies or at the anvil. The optical and synchrotron XPCI images indicate that the first damage appeared as crack onsets similarly inside and on the surface of the specimens. After the 'D' point, two cracks at the opposite free edges initiated and propagated toward the anvil, as shown by the images from the Y-Z-plane at the point 2. At the point 3, part of the 0° plies close to the free edges split, which presumably rotated the specimen and decreased the force measured in the experiments at ESRF. The final shear failure nucleated at the interface between the plies with 0° and ±45° fiber orientations in the middle of the specimen, as marked by red arrows at the point 4. The final fracture propagated in a diagonal direction both inside and on the surface of the specimens. Finally, the specimens disintegrated into two pieces in the in-plane transverse direction, as shown at the point 5 in Fig. 8. It should be noted that the crack nucleates at the free edges by pure compressive shear (the contact is not rigid, when the specimen expands perpendicular to compression). However, after splitting the parts at the edges and slight rotation of the specimen, cracks propagated by local delamination (between layers) and in-plane shear (due to lay-up). At the final failure, a diagonal shear band formed due to the Poisson's effect after lateral deformation (increase of the strain in the transverse in-plane direction). The comparison of the XPCI and optical images revealed that the internal damage initiated and propagated similarly as the crack-front on the specimen surface (i.e., the Y-Z-plane normal to the 0° fiber direction).

3.4. Adiabatic heating at high strain rates

Fig. 9 shows force-strain curve as well as strain and temperature fields of a specimen tested at the strain rate of 1600 s^{-1}. After the 'D' point, the local maximum temperature increased significantly at the free-edge corners of the specimens and exceeded 185 °C, as highlighted by the points 2 and 3. The average surface temperature of the specimen increased only by 20 °C before the peak force, because the heating localized at the edges and the majority of the specimen surface remained

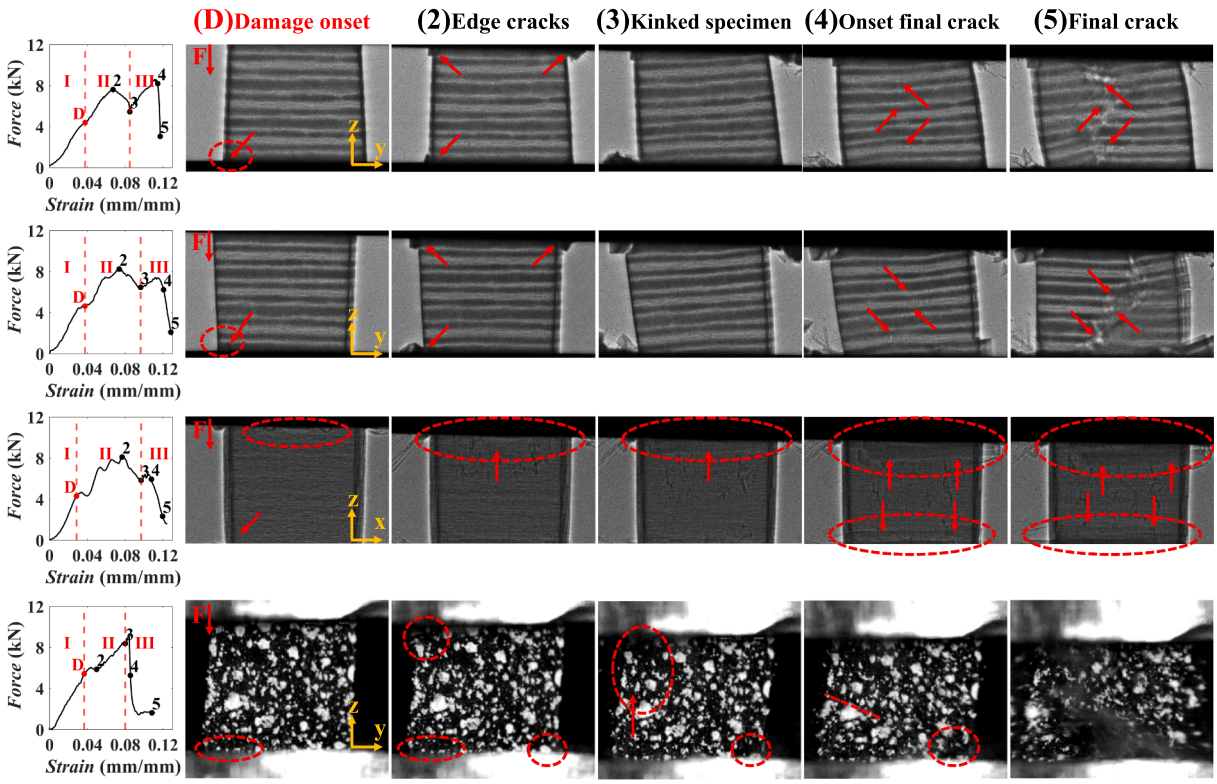

Fig. 8. Damage initiation and propagation in CFRP specimens under dynamic compressive loading at a high strain rate imaged by the synchrotron XPCI from the Y-Z-plane (surface normal to the 0° fiber direction) and the X-Z-plane (normal to the transverse laminate direction) and imaged by the high-speed optical camera from the Y-Z-plane. Note: (1) the loading direction is the vertical direction (red arrow with 'F'), (2) the optical and X-ray images are sorted by the numbering in the force-strain curves on each row. (For interpretation of the references to colour in this figure legend, the reader is referred to the web version of this article.)

close to or at room temperature. After the peak force, the local maximum temperature increased by more than 80 °C simultaneously when the main crack formed through the entire specimen. At the final failure, the heat generation continued and localized at the crack path. The maximum local temperature exceeded 267 °C, but the exact value could not be measured in the experiment because the infrared camera sensor saturated at this temperature level. It should be noted that the current setup is limited in its temperature range and spatial resolution. In future, it may be possible to determine high-speed micro-scale measurements over entire specimen surfaces to detect heating due to fiber, interface, or matrix failure modes.

Fig. 9 (d) indicates the local temperature data over three axial lines, which confirms the strong localization of temperature. At the strain of 0.017 mm/mm, the temperature was 42 C only at the top-left edge of the specimen, indicating that some damage was already accumulating in the specimen before the damage could be observed in the optical or XPCI images. The temperature in the middle of the specimen started to increase at the strain of approximately 0.09 mm/mm. Finally, the temperature in the middle of the specimen was higher compared to the temperature near the edges at the point 4.

3.5. Post-mortem analysis of failure

The damage onset occurred at the free edge of the specimen by shear failure of three plies with 0° fiber orientation in the in-plane transverse direction. This onset phenomenon was observed in both low and high rate tests, and this was supported by in-situ optical and XPCI images. Optical microscope images in Figs. 10 and 11 also confirm this damage at the interface between 0° and −45° plies (third and fourth ply from the free edge). However, this is a post-mortem observation of a fractured specimen after further deformation and damage, and the microscope images do not describe the situation at the damage onset, and therefore clear conclusions about the character of the damage at the damage onset point cannot be made from these images. Figs. 10 and 11 also indicate many cracks with approximately 45° alignment close to the free edge of the specimen, where the damage onset was seen in the optical and XPCI images. This emphasizes the previous note (Sections 3.2 and 3.3) about the failure of specimens by shear crack. For low strain rate tests, matrix cracks in the in-plane transverse direction to the fibers can be observed. For the specimens deformed at a high strain rate, it was possible to image the original damaged surface without cold-mounting and polishing the specimen. Matrix cracks and fiber-matrix debonding were found near the free edge of the specimen deformed at a high strain rate.

Final specimen failure by the diagonal crack was evidenced by optical, XPCI, and thermal images. Each individual ply of the specimens deformed at low strain rates had splitting cracks approximately at an 45° angle, which indicated shear failure of each ply in the in-plane transverse direction. Interestingly, in the specimens deformed at high rates, each individual ply with 0° fiber orientation had splitting cracks similar to transverse failure mode (i.e., tensile load in the direction perpendicular to the compression, due to Poisson's effect). The microscopic failure modes were also studied from SEM images obtained from the middle of the specimen near the main crack, where the highest temperatures were found during the final failure (as seen in Figs. 7 and 9). Fiber breakage was found in many locations near the main diagonal fracture in the specimen deformed at a low rate as shown in Fig. 10. On the other hand, fiber splitting and fiber pull-out as well as fiber breakage were found near the diagonal fracture imaged from the original free surface of the specimen deformed at a high strain rate in Fig. 11.

4. Discussion

The main advantages of this work are the synchronized measurements of the strain and temperature fields describing the deformation

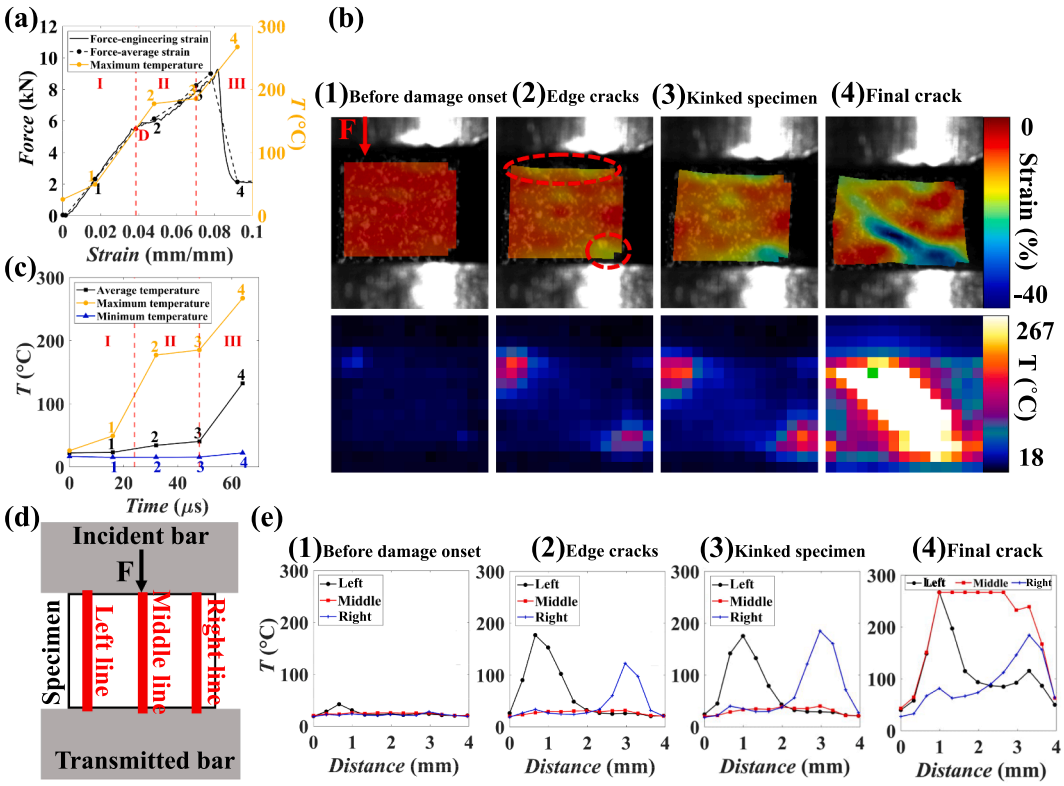

Fig. 9. (a) Force and maximum temperature as a function of strain, (b) full-field strain and temperature maps, (c) average, maximum, and minimum local temperature of the specimen surface as a function of time, (d) position of temperature line profiles, (e) temperature along line profiles indicated in (d) at the strain rate of 1600 s^{-1}. Note: (1) the loading direction is the vertical direction (red arrow with 'F'), (2) the images in (b) and (e) rows correspond to the points marked in graphs (a) and (c). (For interpretation of the references to colour in this figure legend, the reader is referred to the web version of this article.)

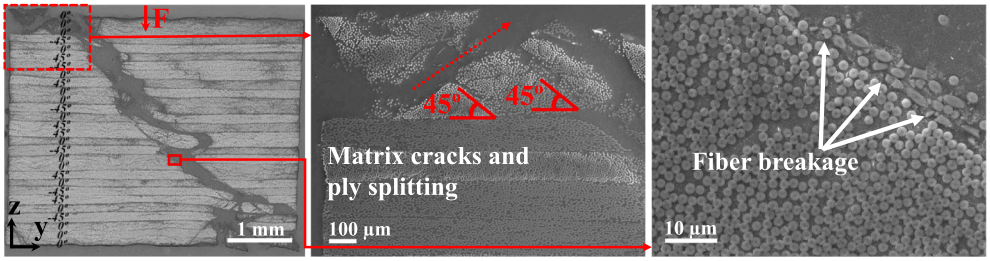

Fig. 10. Optical microscope and SEM images of the damaged specimen deformed at the strain rate of 10^{-3} s^{-1}. Note: the loading direction is the vertical direction (red arrow with 'F'). (For interpretation of the references to colour in this figure legend, the reader is referred to the web version of this article.)

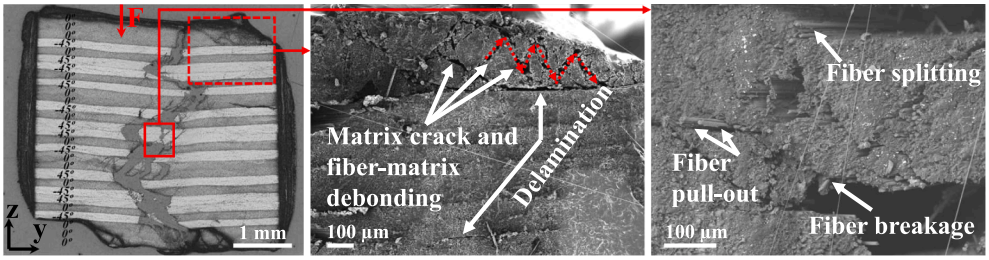

Fig. 11. Optical microscope and SEM images of the damaged specimen deformed at the strain rate of 3000 s^{-1}. Note: the loading direction is the vertical direction (red arrow with 'F'). (For interpretation of the references to colour in this figure legend, the reader is referred to the web version of this article.)

and adiabatic heating of a CFRP laminate specimen during high rate loading. In addition, XPCI was used for the first time to track damage initiation and propagation in the time scale of less than 100 μs for a CFRP laminate under high rate out-of-plane compressive loading. In the study by Li and Lambros [20], a sudden temperature increase of 20 °C occurred when the force dropped abruptly after its peak value. In their work, unidirectional cylindrical CFRP specimens under out-of-plane compression at 1800 s^{-1} were split into two parts along a direction that was about 45° from the axis of compression. However, it was apparent in the current work that the temperature of the CFRP

specimens increased at the damage onset before the peak force. It is important to note that the temperature increases above the T_g at both low and high strain rate experiments after the peak force. Johnston et al. [35] used a high-performance thermal camera to investigate local adiabatic temperature rise of braided composites under ballistic impact. In their study, the local temperature also increased and exceeded the matrix glass transition temperature. This significant temperature rise causes thermal softening in the composite for matrix dominated deformation modes [36,37]. Low rate out-of-plane compression experiments of 3D five-directional braided carbon-epoxy composites have indicated that four symmetric ±45° shear cracks appear in the middle of the composite with a 21° braiding angle, whereas a single 45° shear crack has been observed in the middle of the composite with a 32° braiding angle [38]. When a test was carried out at an initial temperature of 180 °C, small cracks along fiber bundles appeared in the braided composite due to plasticization and decomposition of the matrix. This effect of elevated temperature at low strain rate tests also suggests significant effects of (adiabatic) heating on failure modes at high strain rates. In our work, the strong localization of temperature was observed along the main crack path in the middle of the specimen at both low and high strain rates. In the high strain rate tests, each individual ply with 0° orientation in the middle of the laminate plane was split especially by transverse failure rather than shear failure. In the low rate experiments, the damage in each ply of the laminate resulted in a 45° angle-propagating crack. XPCI data indicated that the internal damage of the specimen was similar to the surface damage seen in the optical images. The XPCI observations also provide a reference for numerical predictions of crack onset and evolution in practical CFRP lay-ups.

5. Conclusions

The adiabatic heating and damage of reinforced carbon-epoxy composite under out-of-plane compression were characterized using high-speed optical, infrared, and synchrotron X-ray phase-contrast imaging. The combination of these experimental methods especially provided an in-situ assessment of surface damage and adiabatic heating as well as an in-situ observation of internal damage evolution in the composite specimens. The findings of this work can be summarized as follows:

- Linear elastic behavior with no observable adiabatic heating before the damage onset was observed during compression tests at all the studied strain rates.
- Combined-data of XPCI and optical imaging revealed that the damage onset occurred at the interface of plies with 0° and −45° fiber orientation near the free edge and propagated by transverse failure of plies, when the specimen was experiencing shear deformation due to Poisson's effect.
- In the high strain rate tests, after the damage onset at the free edges of the specimen, the local temperature significantly increased (exceeding 185 °C). However, in the low strain rate tests, the specimen heated up only after the peak force, when the final crack propagated in the middle of the specimen, as shown in the simultaneous optical and infrared images.
- The main crack formed diagonally through the specimen simultaneously with a sudden decrease in force and an increase in the local temperature. Maximum temperatures of 240 °C were measured in the low strain rate tests, and maximum temperatures exceeding 267 °C were measured in the high rate tests. However, the infrared camera sensor saturated at 267 °C and the true maximum temperature of the specimen in the high rate tests was not obtained.
- The electron microscopy characterization supported the DIC and XPCI results on the micro-scale effects of lay-up damage. In general, highly localized micro-failure was found at the diagonal main crack. In the high strain rate tests, a combination of shear and transverse failure occurred in the middle of the specimen, which affected the main crack path. In the low strain rate tests, essentially pure shear fracture at a 45° angle formed the final crack.

CRediT authorship contribution statement

Nazanin Pournoori: Writing – original draft, Writing – review & editing, Investigation, Validation, Formal analysis, Visualization, Methodology, Software. **Guilherme Corrêa Soares:** Writing – review & editing, Investigation, Formal analysis. **Bratislav Lukić:** Writing – review & editing, Investigation. **Matti Isakov:** Writing – review & editing, Investigation, Software. **Maria Clara Lessa Belone:** Investigation. **Mikko Hokka:** Writing – review & editing, Supervision, Conceptualization, Investigation, Project administration. **Mikko Kanerva:** Writing – review & editing, Supervision, Conceptualization, Project administration.

Declaration of Competing Interest

The authors declare the following financial interests/personal relationships which may be considered as potential competing interests: Nazanin Pournoori reports equipment, drugs, or supplies was provided by Lightweight Structures laboratory of Helsinki University of Technology. Nazanin Pournoori reports equipment, drugs, or supplies was provided by Tampere Microscopy Center facilities at Tampere University.

Data availability

Data will be made available on request.

Acknowledgments

This study was funded by a grant from Tampere University. This work also made use of Tampere Microscopy Center facilities at Tampere University. The XPCI was performed on beamline ID-19 at the European Synchrotron Radiation Facility (ESRF), Grenoble, France with the proposal number MA-5283. The Lightweight Structures laboratory of Helsinki University of Technology is acknowledged for its support with raw materials. Dr. Kati Valtonen is acknowledged for microscopic imaging of the specimens.

Appendix A. Supplementary data

Supplementary data to this article can be found online at https://doi.org/10.1016/j.compositesa.2023.107766.

References

[1] Hsiao HM, Daniel IM. Strain rate behavior of composite materials. Compos Part B Eng 1998;29:521–33.
[2] Tarfaoui M, Choukri S, Neme A. Effect of fibre orientation on mechanical properties of the laminated polymer composites subjected to out-of-plane high strain rate compressive loadings. Compos Sci Technol 2008;68:477–85.
[3] Koerber H, Xavier J, Camanho PP. High strain rate characterisation of unidirectional carbon-epoxy IM7-8552 in transverse compression and in-plane shear using digital image correlation. Mech Mater 2010;42:1004–19.
[4] Okereke MI, Paul Buckley C, Akpoyomare AI. The mechanism of rate-dependent off-axis compression of a low fibre volume fraction thermoplastic matrix composite. Compos Struct 2017;168:685–97.
[5] Griffiths LJ, Martin DJ. A study of the dynamic behaviour of a carbon-fibre composite using the split Hopkinson pressure bar. J Phys D Appl Phys 1974;7:308.
[6] Koerber H, Camanho PP. High strain rate characterisation of unidirectional carbon–epoxy IM7-8552 in longitudinal compression. Compos Part A Appl Sci Manuf 2011;42:462–70.
[7] Cui H, Thomson D, Pellegrino A, Wiegand J, Petrinic N. Effect of strain rate and fibre rotation on the in-plane shear response of ±45° laminates in tension and compression tests. Compos Sci Technol 2016;135:106–15.
[8] Ochola RO, Marcus K, Nurick GN, Franz T. Mechanical behaviour of glass and carbon fibre reinforced composites at varying strain rates. Compos Struct 2004;63:455–67.

[9] Zou H, Yin W, Cai C, Wang B, Liu A, Yang Z, et al. The out-of-plane compression behavior of cross-ply AS4/PEEK thermoplastic composite laminates at high strain rates. Mater 2018;11:2312.
[10] Kobayashi S, Kawahara M. Effects of stacking thickness on the damage behavior in CFRP composite cylinders subjected to out-of-plane loading. Compos Part A Appl Sci Manuf 2012;43:231–7.
[11] Yokozeki T, Kuroda A, Yoshimura A, Ogasawara T, Aoki T. Damage characterization in thin-ply composite laminates under out-of-plane transverse loadings. Compos Struct 2010;93:49–57.
[12] Gao Y, Hu W, Xin S, Sun L. A review of applications of CT imaging on fiber reinforced composites. J Compos Mater 2022;56:133–64.
[13] Garcea SC, Wang Y, Withers PJ. X-ray computed tomography of polymer composites. Compos Sci Technol 2018;156:305–19.
[14] Swolfs Y, Morton H, Scott AE, Gorbatikh L, Reed PAS, Sinclair I, et al. Synchrotron radiation computed tomography for experimental validation of a tensile strength model for unidirectional fibre-reinforced composites. Compos Part A Appl Sci Manuf 2015;77:106–13.
[15] Garcea SC, Sinclair I, Spearing SM, Withers PJ. Mapping fibre failure in situ in carbon fibre reinforced polymers by fast synchrotron X-ray computed tomography. Compos Sci Technol 2017;149:81–9.
[16] Watanabe T, Takeichi Y, Niwa Y, Hojo M, Kimura M. Nanoscale in situ observations of crack initiation and propagation in carbon fiber/epoxy composites using synchrotron radiation X-ray computed tomography. Compos Sci Technol 2020;197.
[17] Garcea SC, Sinclair I, Spearing SM. Fibre failure assessment in carbon fibre reinforced polymers under fatigue loading by synchrotron X-ray computed tomography. Compos Sci Technol 2016;133:157–64.
[18] Gao J, Kedir N, Kirk CD, Hernandez J, Wang J, Paulson S, et al. Real-time damage characterization for GFRCs using high-speed synchrotron X-ray phase contrast imaging. Compos Part B Eng 2021;207:108565.
[19] Gao J, Kedir N, Hernandez JA, Gao J, Horn T, Kim G, et al. Dynamic fracture of glass fiber-reinforced ductile polymer matrix composites and loading rate effect. Compos Part B Eng 2022;235:109754.
[20] Li Z, Lambros J. Dynamic thermomechanical behavior of fiber reinforced composites. Compos Part A Appl Sci Manuf 2000;31:537–47.
[21] Ou Y, Zhu D, Zhang H, Yao Y, Mobasher B, Huang L. Mechanical properties and failure characteristics of CFRP under intermediate strain rates and varying temperatures. Compos Part B Eng 2016;95:123–36.
[22] Meola C, Boccardi S, Carlomagno GM, Boffa ND, Ricci F, Simeoli G, et al. Impact damaging of composites through online monitoring and non-destructive evaluation with infrared thermography. NDT E Int 2017;85:34–42.
[23] Pournoori N, Corrêa Soares G, Orell O, Palola S, Hokka M, Kanerva M. Adiabatic heating and damage onset in a pultruded glass fiber reinforced composite under compressive loading at different strain rates. Int J Impact Eng 2021;147:103728.
[24] Tarfaoui M, El Moumen A, Ben YH. Damage detection versus heat dissipation in E-glass/Epoxy laminated composites under dynamic compression at high strain rate. Compos Struct 2018;186:50–61.
[25] Cohen A, Levi-Hevroni D, Fridman P, Chapman D, Rack A, Olbinado MP, et al. In-situ radiography of a split-Hopkinson bar dynamically loaded materials. J Instrum 2019;14:T06008.
[26] Chen WW, Song B. Split Hopkinson (Kolsky) bar: design, testing and applications. Springer Science & Business Media; 2010.
[27] Soares GC, Vázquez-Fernández NI, Hokka M. Thermomechanical Behavior of Steels in Tension Studied with Synchronized Full-Field Deformation and Temperature Measurements. Exp Tech 2021;45:627–43.
[28] Weitkamp T, Tafforeau P, Boller E, Cloetens P, Valade JP, Bernard P, et al. Status and evolution of the ESRF beamline ID19. AIP Conference Proceedings 2010;1221:33.
[29] Rack A, Scheel M, Hardy L, Curfs C, Bonnin A, Reichert H. Exploiting coherence for real-time studies by single-bunch imaging. J Synchrotron Radiat 2014;21:815–8.
[30] Kuroda R, Sugawa S. A high sensitivity 20Mfps CMOS image sensor with readout speed of 1Tpixel/sec for visualization of ultra-high speed phenomena. In selected papers from the 31st International Congress on High-Speed Imaging and Photonics 2017;10328:1032802.
[31] Lukić B, Saletti D, Forquin P, Blasone M, Cohen A, Rack A. Single Bunch X-Ray Phase-Contrast Imaging of Dynamic Tensile Failure in Geomaterials. J Dzn Behav Mater 2022;1:13.
[32] Skytta V, Saarela O, Wallin M. Progressive failure of composite laminates; analysis vs experiments. In Fracture of Nano and Engineering Materials and Structures: Proceedings of the 16th European Conference of Fracture, Alexandroupolis, Greece, 2006:341-42.
[33] Asseff NS, Mahfuz H. Design and finite element analysis of an ocean current turbine blade. IEEE 2009 Oct 26.
[34] Hosur MV, Alexander J, Vaidya UK, Jeelani S, Mayer A. High Strain Rate Compression Characterization of Affordable Woven Carbon/Epoxy Composites under off-Axis Loading. Polym Polym Compos 2003;11:527–39.
[35] Johnston JP, Pereira JM, Ruggeri CR, Roberts GD. High-speed infrared thermal imaging during ballistic impact of triaxially braided composites. J Compos Mater 2018;52:3549–62.
[36] Garg M, Mulliken AD, Boyce MC. Temperature rise in polymeric materials during high rate deformation. J Appl Mech Trans ASME 2008;75:0110091–8.
[37] Sorini C, Chattopadhyay A, Goldberg RK. An improved plastically dilatant unified viscoplastic constitutive formulation for multiscale analysis of polymer matrix composites under high strain rate loading. Compos Part B Eng 2020;184:107669.
[38] Zuo HM, Li DS, Jiang L. High temperature mechanical response and failure analysis of 3D five-directional braided composites with different braiding angles. Materials 2019;12(21):3506.